High-Temperature Decomposition of Diisopropyl Methylphosphonate (DIMP) on Alumina: Mechanistic Predictions from Ab Initio Molecular Dynamics

Sohag Biswas and Bryan M. Wong*

Department of Chemical & Environmental Engineering, Materials Science & Engineering Program, Department of Physics & Astronomy, and Department of Chemistry, University of California-Riverside, Riverside, California 92521, USA

E-mail: bryan.wong@ucr.edu,Website:http://www.bmwong-group.com

Abstract

The enhanced degradation of organophosphorous-based chemical warfare agents (CWAs) on metal-oxide surfaces holds immense promise for neutralization efforts; however, the underlying mechanisms in this process remain poorly understood. We utilize large-scale quantum calculations for the first time to probe the high-temperature degradation of diisopropyl methylphosphonate (DIMP), a nerve agent simulant. Our Born-Oppenheimer molecular dynamics (BOMD) calculations show that the γ-Al_2O_3 surface shows immense promise for quickly adsorbing and destroying CWAs. We find that the alumina surface quickly adsorbs DIMP at all temperatures, and subsequent decomposition of DIMP proceeds via a propene elimination. Our BOMD calculations are complemented with metadynamics simulations to produce free energy paths, which

show that the activation barrier decreases with temperature and DIMP readily decomposes on γ-Al_2O_3. Our first-principle BOMD and metadynamics simulations provide crucial diagnostics for sarin decomposition models and mechanistic information for examining CWA decomposition reactions on other candidate metal oxide surfaces.

Introduction

The neutralization of chemical warfare agents (CWAs) continues to be a pressing area of interest for the safe and effective removal of these hazardous compounds. Among the various CWAs, the most nefarious are organophosphate nerve agents (such as sarin), which contain P=O, P–O–C, and P–C bonds that enable lethal phosphorylating mechanisms.[1] Over the past few decades, a variety of destruction and neutralization methods have been used to safely eliminate these hazardous compounds. For example, destruction-based methods (typically pyrolysis) allow a one-step approach for the complete disposal of CWAs at the expense of using specialized equipment under extreme conditions.[1,2] On the other hand, neutralization methods offer potentially reversible chemical treatments, leading to possible CWA precursors under less severe conditions.[1]

Recent studies have shown that metal oxides can effectively destroy CWAs due to their high surface area, a large number of highly reactive edges, corner defect sites, unusual lattice planes, and high surface-to-volume ratios. In particular, metal oxides, such as CaO,[3,4] MgO,[5,6] ZnO,[7–9] TiO_2,[10–16] Al_2O_3,[17–20] Fe_3O_4,[21] and CuO[22] are candidates as adsorbents for enhancing the decomposition of CWAs. In γ-Al_2O_3, Al atoms in the bulk exhibit either a tetrahedral or octahedral coordination. However, depending on the exposed crystallographic surface, Al atoms on the surface can display penta-, tetra, and tri-coordination and exhibit Lewis acidity.[23–26] Because of its high degree of surface heterogeneity, γ-Al_2O_3 offers a high catalytic activity and is a promising candidate for the decomposition of various CWAs.[27]

In this work, we present the first *ab initio* molecular dynamics study for probing high-temperature decomposition dynamics of diisopropyl methylphosphonate (DIMP) on the γ-

Al_2O_3 surface. Due to its structural similarity with sarin, DIMP has been used in experiments to mimic the decomposition reaction mechanism of CWAs. DIMP is the only surrogate with the same isopropyl (–O–C_3H_7) group found in sarin gas (the only structural difference between sarin and DIMP is the substitution of a fluorine for an isopropyl group in the former). Several techniques have also been used to probe DIMP decomposition, including microwave discharge approaches,[28] pyrolysis on porous substrates,[29] laser heating,[30] and thermal decomposition at 700 – 800 K.[31] Despite these experimental studies, theoretical analyses of DIMP decomposition on metal oxides are scarce, except for a previous study on mechanism and rates of thermal decomposition of DIMP.[32] In this work, we utilize large-scale *ab initio* molecular dynamics simulations to probe the adsorption dynamics and time scales of DIMP decomposition at various temperatures. In addition, we present new *ab initio*-based metadynamics simulations to calculate free-energy barriers for various bond breaking decomposition reactions of DIMP. These computational techniques allow us to (1) predict activation energies and detailed mechanistic pathways at various temperatures and (2) establish accurate sarin decomposition models on metal-oxide surfaces to guide experimental efforts for neutralizing DIMP.

Simulation Details

Molecular Dynamics Simulations

Density functional theory (DFT) based Born-Oppenheimer molecular dynamics (BOMD) simulations were carried out using the CP2K[33] software suite. We have specifically chosen to use this software package since the implementation of linear-scaling Kohn-Sham approaches in CP2K allows robust and efficient electronic structure calculations for large systems. The Perdew-Burke-Ernzerhof (PBE)[34] was used for the DFT calculations with Grimmes's D3 method to account for dispersion forces.[35] To obtain reasonable accuracy, we utilized a DZVP (double zeta valence polarized) basis set for Al in the DFT calculations and the

TZV2P basis set for C, O, H, and P atoms with the Goedecker, Teter, and Hutter (GTH) pseudopotentials[36,37] for atomic core electrons. A similar basis set for Al atoms was also used to accurately calculate methane activation[38] and alkane dehydrogenation[39] on the γ-Al_2O_3 surface. The orbital transformation method with an electronic gradient tolerance value of 1×10^{-5} atomic units was adopted as the convergence criteria for the SCF cycle.[40] A kinetic energy cut-off of 400 Ry for the auxiliary plane-wave basis with a 0.5 fs timestep was employed to integrate the equations of motion. The initial guess was furnished by the stable predictor-corrector extrapolation method at each molecular dynamics step.[41,42] We have carried out several molecular dynamics simulations in the 200 – 1000° C temperature range in increments of 100° C (i.e., a total of nine independent trajectories were considered). All simulations were carried out using a Nose-Hoover chain thermostat with the canonical

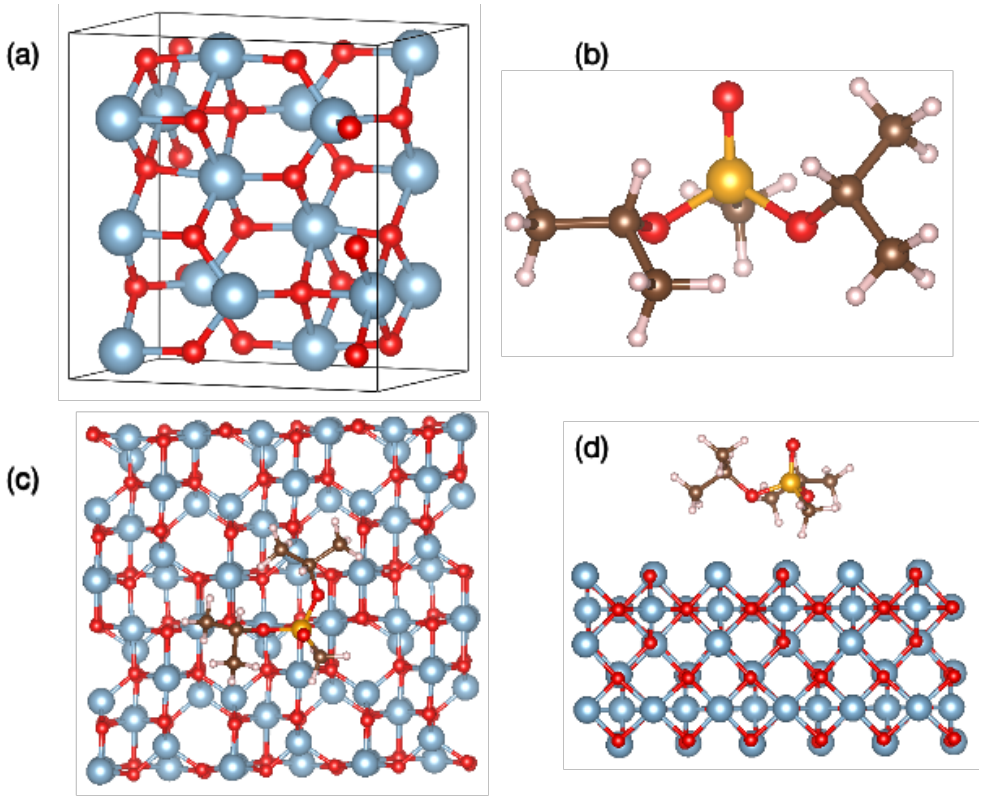

Figure 1: (a) Bulk structure of γ-Al_2O_3. (b) Molecular structure of diisopropyl-methylphosphonate (DIMP). (c) Top view of DIMP adsorbed on the γ-Al_2O_3 surface. (d) Side view of DIMP adsorbed on the γ-Al_2O_3 surface. The blue, red, orange, brown, and light pink spheres represent Al, O, P, C, and H atoms, respectively.

ensemble (NVT).[43,44]

The nonspinel model of the bulk γ-alumina unit cell (shown in Figure 1a) was built using the crystallographic model by Dinge et al.,[23,45] which has been shown to match well with experimental structural parameters.[46] Our calculated cell parameters ($a = 7.90$ Å, $b = 7.93$ Å, and $c = 8.07$ Å)[23,45] for bulk γ-alumina are in excellent agreement and within 2% of the experimental cell parameters ($a = b = 7.96$ Å and $c = 7.81$ Å).[46] In our simulations, we used the (100) facet of this model, which is the lowest-energy facet reported for this material.[23] It is worth mentioning that our calculations represent a simplified model of the metal-oxide surface, and impurities (such as H_2O, OH, SOx, etc.) may be present and play a crucial role in its reactivity. Nevertheless, our large-scale BOMD calculations still provide critical atomistic insight into the reactivity of the original pristine material, which serves as a baseline for comparing its catalytic activity against other mixed metal oxide surfaces (and their associated impurities), which we save for future studies.

For our NVT simulations, a $3 \times 1 \times 2$ supercell of γ-alumina and a single DIMP molecule (Figure 1b) containing a total of 268 atoms were used. We introduced a single DIMP molecule 5 – 6 Å above the center of the alumina slab along the y-direction, as shown in Figure 1c. Periodic boundary conditions were applied in the x and z directions. Thus, the xz plane of the slab is parallel to the surface, and the y-axis forms the surface normal where DIMP interacts with the alumina surface. We introduced a vacuum layer of 15 Å on top of the surface to avoid any significant overlap between the electronic density of periodically translated cells. Our BOMD simulations show that the DIMP molecule moves extremely fast and explores a large space of configurations. To limit this exploration to regions where DIMP dissociation on alumina might occur, it is essential to restrict the movement of the DIMP molecule. Specifically, an external spherical potential, which only acts on the DIMP molecule, was placed at the center of the system. Due to the computationally expensive nature of these simulations, we performed 12 ps NVT simulations for each trajectory. We also calculated adsorption energies using conventional geometry optimizations using the Broyden-Fletcher-

Gold-farb-Shanno (BFGS) minimization algorithm until the forces converged to 4.0×10^{-4} Bohr with an SCF convergence criteria of 1×10^{-5} au. For the geometry optimization, we used a relatively small supercell ($1 \times 2 \times 2$) compared to our BOMD simulations.

Metadynamics Simulations

Throughout our BOMD simulations, we did not observe any decomposition of DIMP on alumina within the 200 – 600° C temperature range (decomposition did occur at higher temperatures, which is discussed later in this paper). At lower temperatures, the high computational cost of these simulations only permits explorations of short time intervals; therefore, BOMD simulations alone do not permit a routine exploration of the complete reaction dynamics. One can sidestep this limitation by using advanced computational techniques such as metadynamics simulations (MetaD),[47] which we describe further below. In short, MetaD bypasses the sampling limitations of traditional molecular dynamics by applying a history-dependent biasing potential as a function of time to enable efficient sampling of the free energy surface. The free energy surface itself is defined over a set of collective variables (CVs), which are carefully chosen to provide a complete description of the system's slow degrees of freedom. The decomposition process is characterized by the breaking of various bonds within the DIMP molecule on the alumina surface. For this reason, we utilized two CVs, shown in Figure 2, for our accelerated sampling simulations. The CV specifies the coordination number (CN) during the MetaD simulations, which is expressed as a function of the distance between two atoms:

$$\text{CV or CN} = \frac{1 - \left(\frac{d_{\text{AB}}}{d_0}\right)^p}{1 - \left(\frac{d_{\text{AB}}}{d_0}\right)^{p+q}}, \tag{1}$$

where d_{AB} is the distance between atoms A and B, and d_0 is the reference distance or fixed cut-off parameter (this parameter characterizes the standard bond distance between atoms A and B). The variables p and q in Equation 1 are constants, which were fixed to $p = q = 6$.

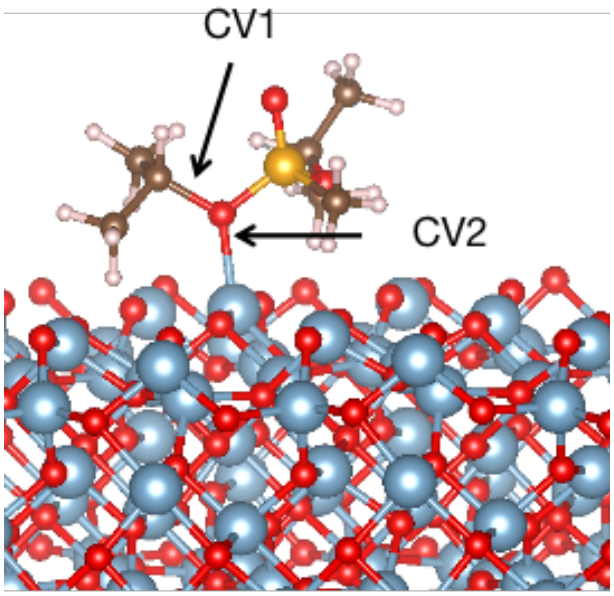

Figure 2: Collective variables (CVs) used to describe the adsorption dynamics of DIMP on the alumina surface.

In this work, we chose CV1 to be the distance between the C and O atoms within DIMP, and CV2 as the distance between the O atom in DIMP and an Al atom on the alumina surface, as shown in Figure 2. MetaD simulations were carried out by depositing Gaussians with heights of 0.02 and 0.001 Hartree for the 200 – 500° C and 600 – 1000° C temperature ranges, respectively. The widths of the Gaussians were set to 0.1 for both the CV1 and CV2 simulations. In this work, well-tempered MetaD (wt-MetaD) simulations were used[48,49] with the deposition rate of the Gaussian hills set to 20 steps. The well-tempering was implemented using a Gaussian height damping factor of ΔT such that the ratio $\frac{\Delta T+T}{T}$ was equal to 6. We performed two sets of wt-MetaD simulations for each temperature from different initial conditions, which were extracted from the pre-equilibrated BOMD simulations. We confirmed a representative sampling and convergence of the reactant, product, transition state, and free energy differences, particularly for the dissociation of the C–O bond in DIMP on the alumina surface.

Results and Discussions

Adsorption of DIMP on the Alumina Surface

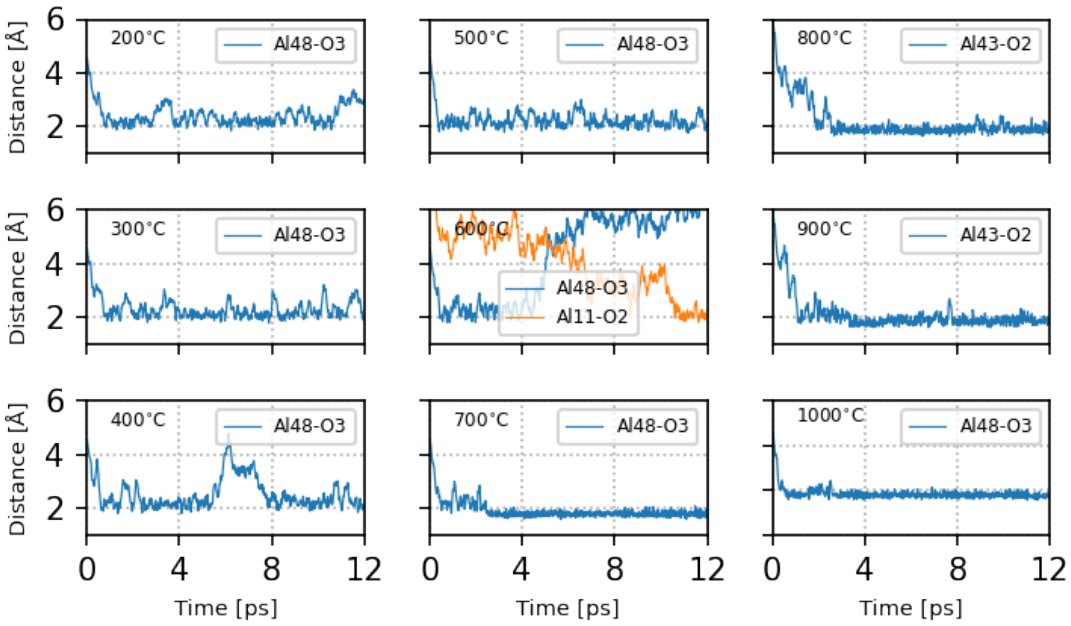

Figure 3: Time-dependent fluctuations of various Al–O distances, which confirm DIMP adsorption throughout the BOMD simulations for all temperatures.

Metal oxide surfaces are typically catalytic and can adsorb and subsequently decompose CWAs into benign products. Prior experiments[50] and theoretical[27] calculations have shown that sarin simulants can adsorb on metal oxides by forming a bond with metal atoms via a phosphoryl oxygen. Initially, we observed the DIMP molecule interacting with an Al atom via the O atom of the P–OC_3H_7 moiety. To further explore these dynamical effects with our BOMD simulations, Figure 3 plots the distance between one of the surface Al atoms and the oxygen of the P–OC_3H_7 moiety in DIMP at various temperatures. These calculations show that DIMP adsorption occurs within two picoseconds for all temperatures, and the oxygen of the P–OC_3H_7 moiety of DIMP interacts with the tetra-coordinated Al center. We did not observe any desorption of DIMP on the alumina surface, as indicated by the small Al48–O3 bond distances in Figure 3 (as a side note, the 600° C plot in the center of Figure 3 does show

dissociation of the Al48–O3 bond, but a new Al11–O2 bond quickly forms thereafter, and the DIMP molecule still remains on the alumina surface). Figure 4 shows snapshots from our simulations depicting various DIMP adsorption configurations on the alumina surface. As suggested by prior theoretical calculations,[51–53] the adsorption via the O atom of the P–OC_3H_7 moiety is crucial for propene elimination. As the MD simulations progresses, we also observe interactions between the O (in the –P=O group) and Al atoms. In short, the DIMP molecule remained adsorbed on the alumina surface in our simulations for all temperatures.

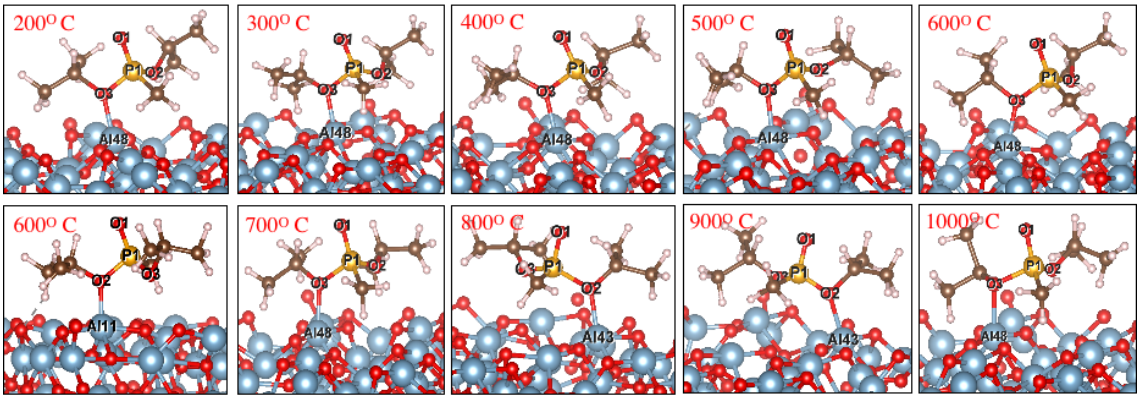

Figure 4: Snapshots illustrating the adsorption of DIMP on the alumina surface. From 200 – 500° C, adsorption occurs via the formation of the Al48–O3 bond. At 600° C, adsorption proceeds via the formation of the Al48–O3 and Al11–O2 bonds. At 700 and 1000° C, the Al48–O3 bond is formed during the adsorption process, and from 800 – 900° C, an Al43–O2 bond is formed.

To complement our MetaD simulations, we also calculated adsorption energies, E_{ads}, using the following expression:

$$E_{\text{ads}} = E_{\text{DIMP+surface}} - E_{\text{surface}} - E_{\text{DIMP}}, \tag{2}$$

where E_{surface} is the energy of the alumina surface, E_{DIMP} is the energy of an isolated gas-phase DIMP molecule, and $E_{\text{DIMP + surface}}$ represents the energy of the adsorbed molecule on the surface. A negative value of E_{ads} corresponds to an exothermic process and a stable adsorption configuration. The tri-coordinated Al surface atoms are known to be strong Lewis

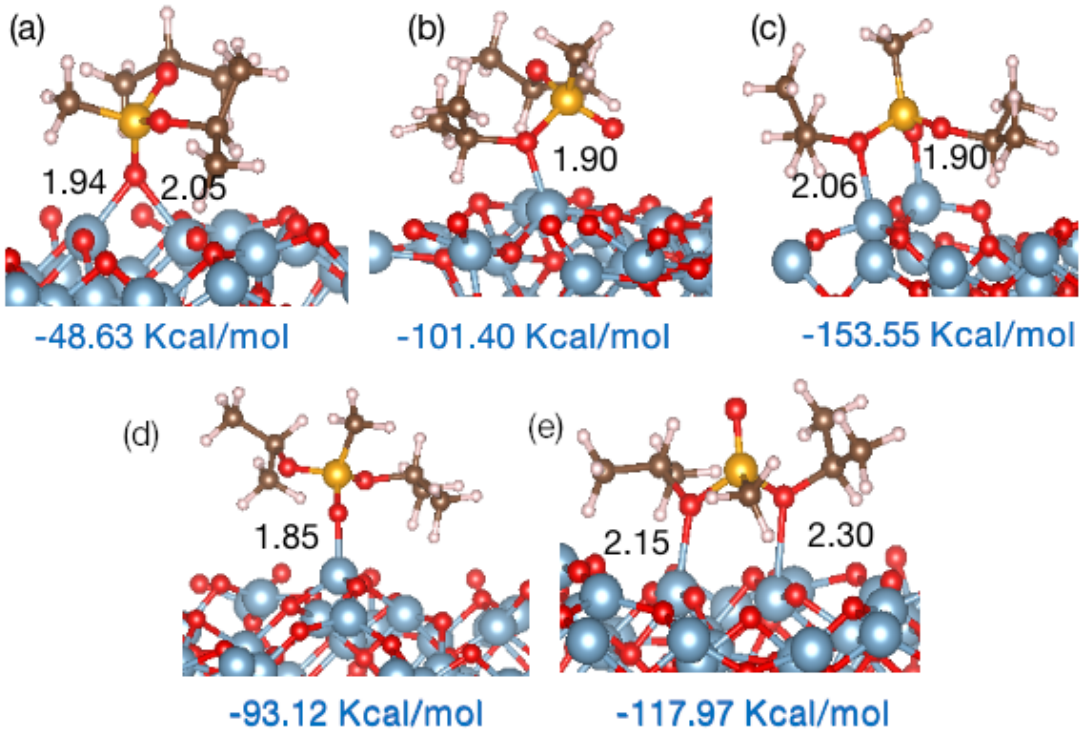

Figure 5: Various adsorption configurations of DIMP on the γ-Al_2O_3 (100) surface. Bond distances are shown in angstroms.

acid-type catalytic sites[54] and give large adsorption energies when the DIMP molecule binds to them. Figure 5 illustrates selected optimized structures of DIMP on the alumina surface. In panel 5(a), the DIMP molecule is bonded to two tetra-coordinated Al atoms via the phosphoryl oxygen, resulting in a bridging adsorption with $E_{\text{ads}} = -48.63$ kcal/mol. In panel 5(b), the alkoxy oxygen is bonded to a tri-coordinated Al atom, giving an adsorption energy of -101.40 kcal/mol. The largest adsorption energy (-153.55 kcal/mol) was obtained for the configuration shown in panel 5(c) where the alkoxy and phosphoryl oxygen atoms are bonded to two different tri-coordinated Al centers. In panel 5(d), the phosphoryl oxygen is bonded to a tri-coordinated Al center, giving an adsorption energy of -93.12 kcal/mol. The adsorption energy for configuration in panel 5(e) is -117.97 kcal/mol in which the DIMP molecule binds with two tetra-coordinated Al atoms via two alkoxy oxygen atoms. Our calculated adsorption energy for the configuration shown in panel 5(a) is in good agreement with a previously studied similar configuration of sarin adsorption on γ-Al_2O_3 (-49.2 kcal/mol).[27]

Decomposition of DIMP on the Alumina Surface

We next examine DIMP decomposition mechanisms on the alumina surface. Previous studies have shown that one of the decomposition pathways of DIMP proceeds through the breaking of a C–O bond.[28] Figure 6a displays time-dependent variations of C–O bond distances from 200 – 600° C, which fluctuate around 1.50 Å (the covalent C–O bond distance), indicating that the C–O bond remains intact. On the other hand, Figure 6b shows that when the temperature is raised to 700 – 1000° C, the C–O bond lengthens significantly, signifying decomposition. It is worth noting that the timescales for DIMP decomposition varies with temperature, and we observe a very rapid decomposition at 1000° C.

Figure 7 depicts snapshots at crucial points for the decomposition of DIMP on the alumina surface for a few representative MD trajectories. As mentioned in the previous section, adsorption initially occurs via the oxygen atom of the P–OC_3H_7 moiety in DIMP and an Al atom on the alumina surface (which occurs at all temperatures). At 700° C, the 3 panels

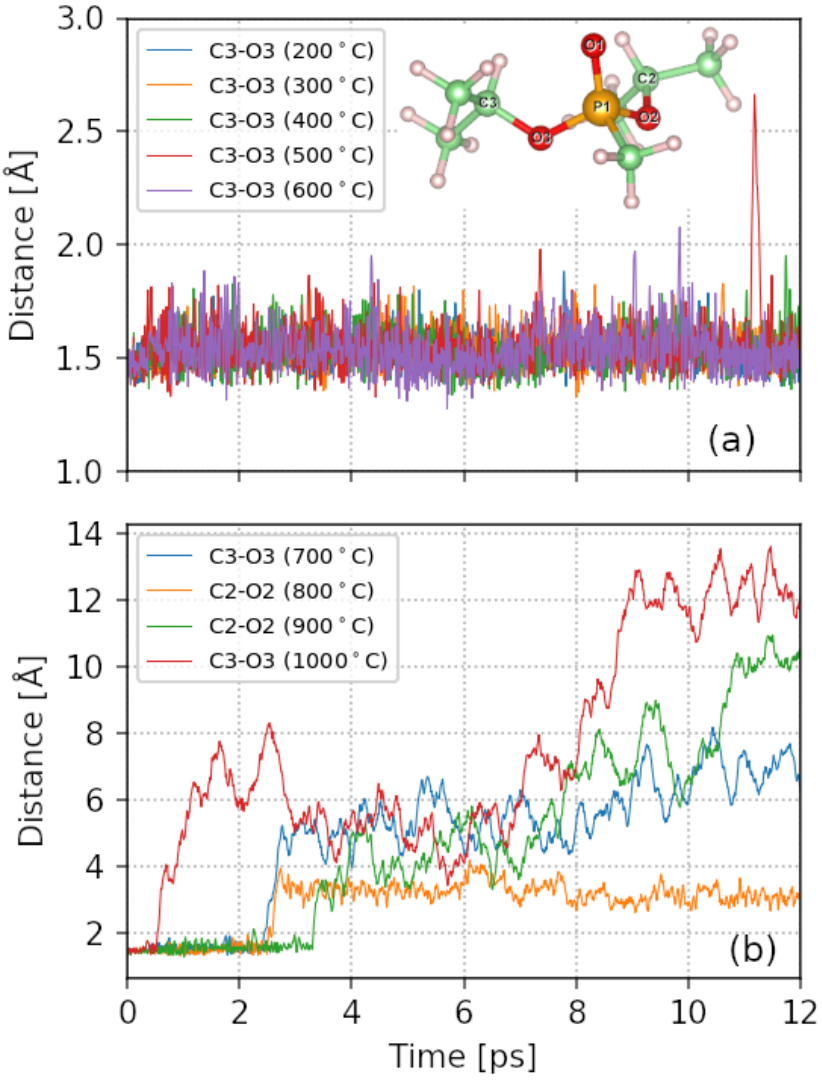

Figure 6: Evolution of C–O distances as a function of time on the alumina surface at various temperatures, which describes DIMP decomposition. The corresponding atom labeling is shown in the inset panel of (a).

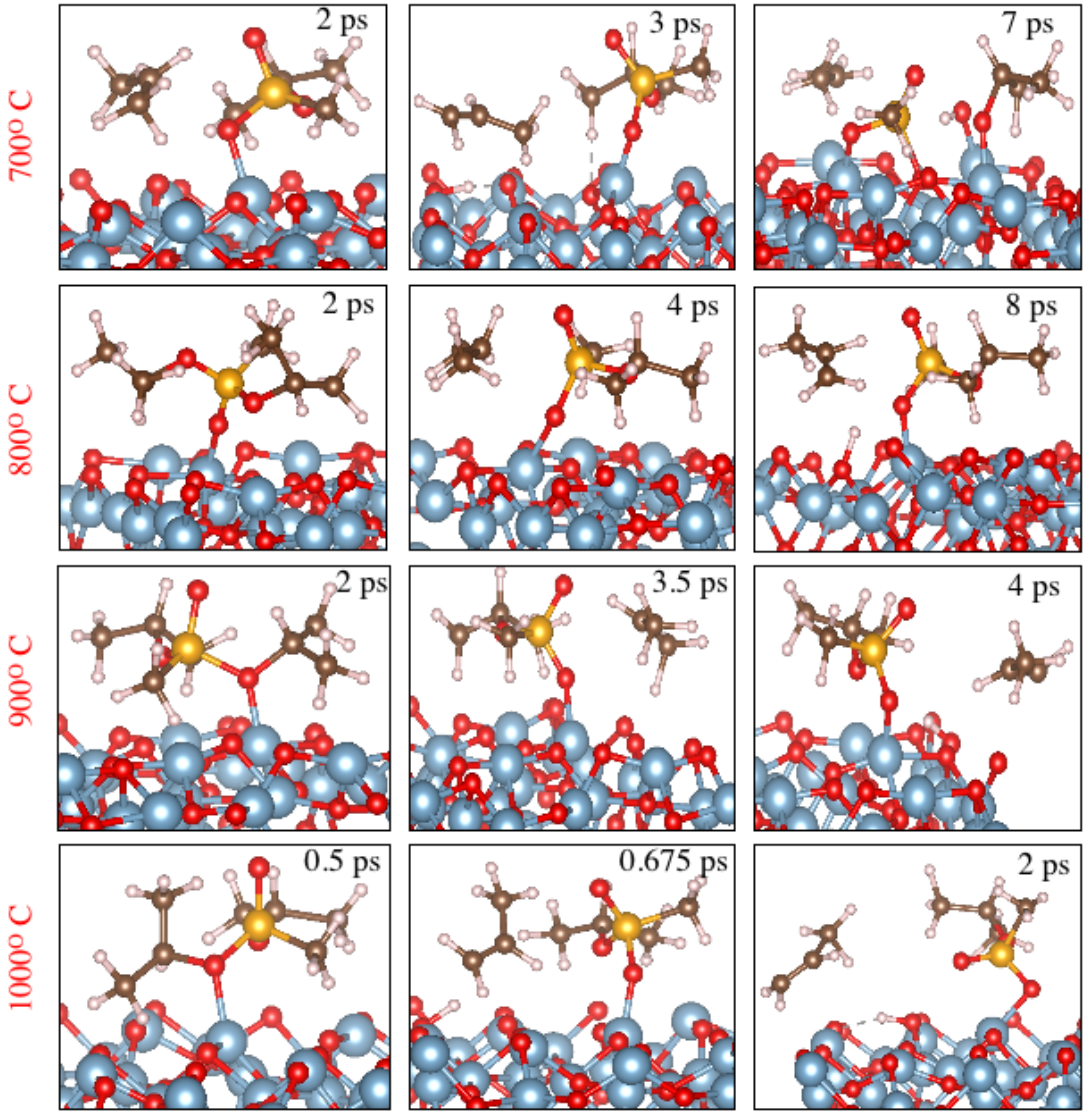

Figure 7: Snapshots of DIMP decomposition from representative MD trajectories at various temperatures.

at the top of Figure 7 depict a possible decomposition pathway in which the C3–O3 bond breaks after 2 ps and an Al–O bond forms with the alumina surface. During this process, a surface-bound n-alkyl ($–C_3H_7$) species is formed. At ∼3 ps, a single terminal C–H bond from the n-alkyl molecule is broken when a proton is abstracted by an oxygen atom on the alumina surface. This forms propene, an unsaturated compound, as a by-product. As the simulation further proceeds, the P–O bond in DIMP dissociates at 7 ps and forms a new Al–$OCHCH_3CH_3$ adsorbate on the alumina surface. In addition, once the P–O bond in DIMP is cleaved, a new P–O bond is formed between the phosphorus atom and a di-coordinated surface oxygen atom (see the 3 panels at the top of Figure 7). At 800 – 1000° C (depicted in the bottom 9 panels of Figure 7), DIMP decomposition involves only the propene elimination via a two-step process. The first step of the propene elimination is associated with the dissociation of the C2–O2 (800 – 900° C) or C3–O3 (1000° C) bond. The second step comprises the migration of the hydrogen atom from the methyl group of the $–C_3H_7$ fragment to one of the surface oxygen atoms. Within these simulated timescales, we did not observe any further decomposition of DIMP within the 800 – 1000° C temperature range.

Free energy profiles

The propene end-products predicted by our BOMD simulations corroborates previous experiments on DIMP, which include thermal decomposition studies,[55,56] pyrolysis and combustion in nitrogen/oxygen-rich environments,[57] as well as microwave[28] and laser-induced[30] decomposition under inert environments. Collectively, all of these prior experimental studies detected propene as one of the main by-products of DIMP decomposition, which further supports our BOMD predictions. To further investigate the decomposition of DIMP on alumina, we utilized well-tempered metadynamics simulations by adopting two collective variables. We performed two sets of metadynamics simulations (for each temperature within the 200 – 1000° C range) using different initial conditions. Obtaining accurate free energy profiles from metadynamics simulations requires (1) longer simulation times until all acces-

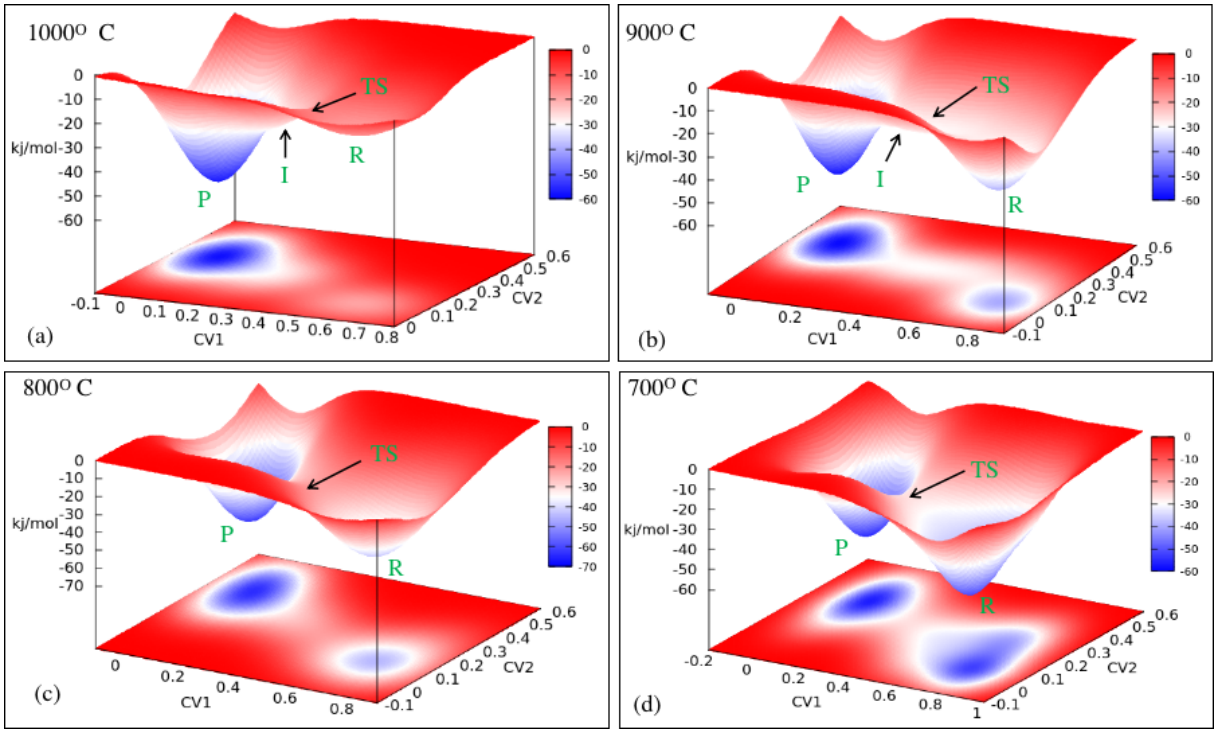

Figure 8: Reconstructed free energy surface for the decomposition of DIMP on the alumina surface at (a) 1000° C, (b) 900° C, (c) 800° C, and (d) 700° C. The R, TS, I, and P labels in each free energy surface correspond to the reactant, transition state, intermediate, and product, respectively.

sible regions of the potential are explored (with trajectories spanning forward and backward many times between reactant and product states) and (2) a careful selection of collective variables. Our well-tempered metadynamics simulations at various temperatures suggests that when the C–O bond is broken, subsequent reforming of this bond is prohibited (Figure S19), which indicates that the reaction is irreversible. The Supporting Information (Figures S20 and S21) provides further details on the convergence of our free energy profiles between the transition state and reactant basin as a function of time, which demonstrates that our metadynamics simulations are fully converged.

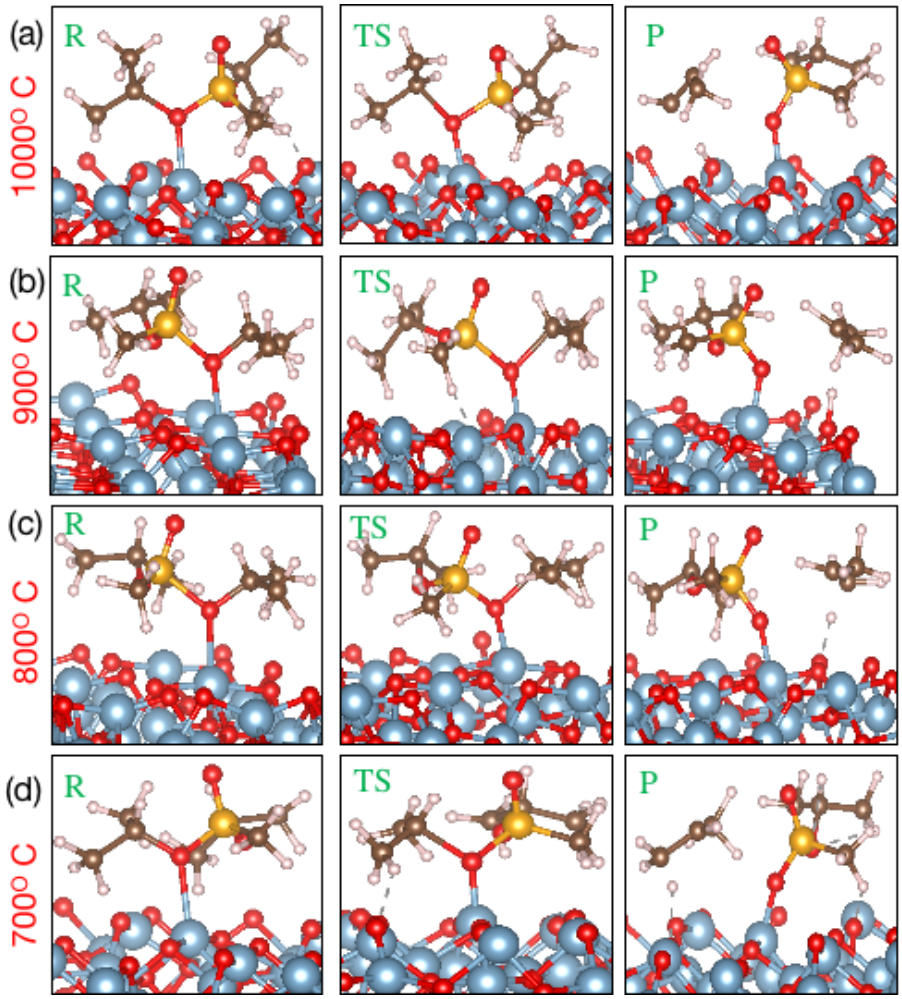

Figure 9: Snapshots from the well-tempered metadynamics simulations within the 700 – 1000° C temperature range. The R, TS, and P labels illustrate the reactant, transition state, and product, respectively.

The free energy surface at 1000° C is shown in Figure 8 (a). The two CVs that capture

the energetics of DIMP decomposition are presented in Figure S1. In this mechanism, the reactant (R) goes to a product (P) via a transition state (TS) and a small tiny intermediate (I) in between the transition state and product. The reactant state is defined by CV1 = 0.75 (C–O = 1.66 Å) and CV2 = 0.11 (Al–O = 2.17 Å), where DIMP is bonded to the surface Al atom. The decomposed DIMP product, P, is characterized by CV1 = 0.03 (C–O = 3.12 Å) and CV2 = 0.40 (Al–O = 1.77 Å), in which the C–O bond of DIMP is cleaved. At this stage, the H atom from the $–C_3H_7$ moiety is transferred to a surface oxygen atom, and propene is formed. The C–O bond length stretches to 1.87 Å at the transition state (which has an activation barrier of only 4.11 kJ/mol) and subsequently dissociates. The reactant, transition state, and product from our well-tempered metadynamics simulations at 1000° C are shown in Figure 9(a). In the Supplementary Material, we provide an additional free energy profile (Figure S2) at 1000° C that utilizes different initial conditions. For this separate case, the reactant proceeds to the product state via a stable transition state with a tiny minimum, and the activation barrier is ∼6.36 kJ/mol. Collectively, the average free energy value from these independent trajectories is 5.24 kJ/mol.

The reaction mechanism at 900° C is very similar to that of 1000° C, which also shows a tiny intermediate between the product and transition state, as shown in Figure 8(b). The free energy barrier value is ∼11.85 kJ/mol, and Figure S3 in the Supplementary Material shows the corresponding evolution of CV1 and CV2. The geometries of the reactant, transition state, and product along the metadynamics trajectory are reported in Figure 9(b). We have also performed additional metadynamics calculations using different initial conditions to test the reproducibility of these results. In these additional calculations (depicted in Figure S4 in the Supplementary Information), the reactant proceeds to the product through a single transition state with a free energy barrier value of ∼15.73 kJ/mol. The average free energy barrier value obtained from these different initial conditions is 13.79 kJ/mol.

The reconstructed free energy surfaces at 800 and 700° C are shown in Figures 8(c) and 8(d), and fluctuations of the corresponding CV values are presented in Figures S5 and S6,

respectively. In contrast to the higher temperatures discussed previously, the decomposition of DIMP at 800 and 700° C proceeds via a single transition state. At 800° C, the collective variables CV1 (0.71) and CV2 (0.12) define the reactant state R, at which DIMP forms a bond with the surface Al atom (typical C–O and Al–O bond distances at this geometry are 1.53 and 2.25 Å, respectively). The C–O bond in DIMP stretches to 1.91 Å to form a transition state, and the reaction progresses to the product where the C–O bond subsequently dissociates, and propene is formed. The net free energy barrier for this activation process is ∼22.53 kJ/mol. The additional free energy profile at 800° C from the different initial conditions is shown in Figure S7. A very similar reaction mechanism is also observed at 700° C with a slightly higher activation barrier of ∼26.65 kJ/mol. Figure S8 in the Supplementary Material represents the topology of another free energy surface at 700° C from different initial conditions. The reactant, transition state, and product geometries from these metadynamics simulations are shown in Figures 9(c) and 9(d) for 800 and 700° C, respectively. A detailed analysis of

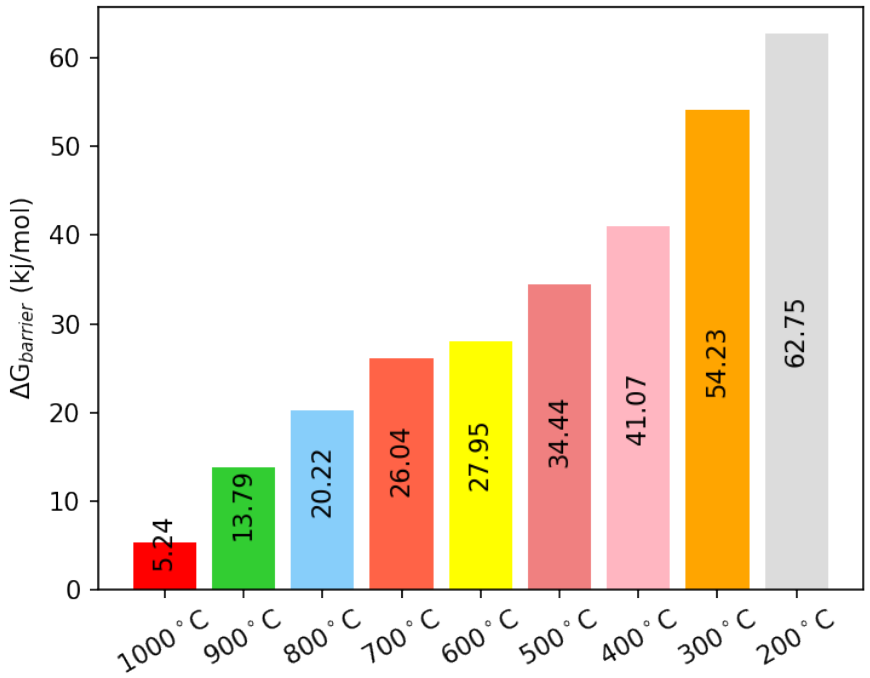

Figure 10: Free energy activation barrier as a function of temperature for the decomposition of DIMP on the alumina surface. The free energy activation barrier value is calculated by averaging over two metadynamics simulations at each temperature.

free energy profiles for DIMP decomposition on alumina at various temperatures (200 – 600° C) with different initial conditions is given in the Supplementary Material (Figures S9-S18). Figure 10 summarizes the free energy activation barrier as a function of temperature, which shows that the free energy activation barrier decreases with temperature. Static DFT calculations have obtained free energy activation barrier values of 113 kJ/mol (ZnO surface),[51] 108.0 kJ/mol (rutile surface),[53] 122.6 kJ/mol (anatase surface),[53] and 53.7 kJ/mol (MoO_2 surface).[52] However, the free energy activation barriers for C–O bond breaking from our simulations are much lower than these previously reported values. We also note that the free energy activation barrier value at 600° C is very similar to that of 700° C.

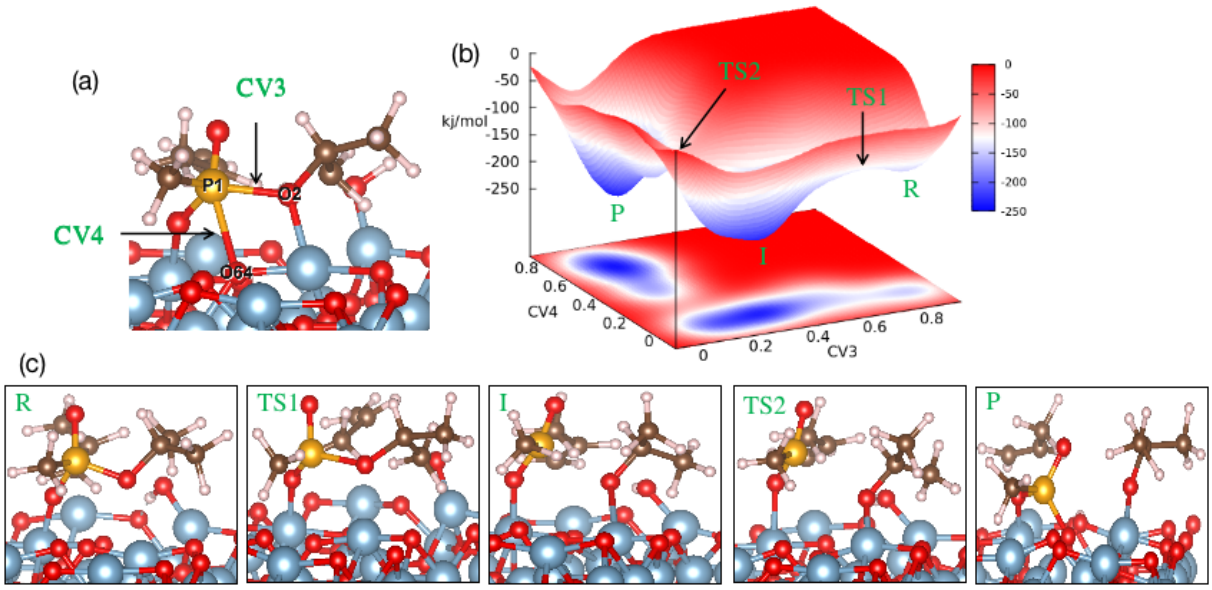

Figure 11: Panel (a) depicts collective variables used in studying the formation of an Al–$OCHCH_3CH_3$ adsorbate at 700° C, and panel (b) shows the 3D reconstructed free energy surface, where R, TS1, I, TS2, and P correspond to the reactant, transition state 1, intermediate, transition state 2, and product, respectively. Panel (c) shows snapshots of R, TS1, I, TS2, and P along the metadynamics trajectory.

At 700° C, we observed formation of an Al–$OCHCH_3CH_3$ adsorbate in addition to propene. To further analyze these energetics with metadynamics simulations, we utilized two collective variables: CV3 [P1–O2] and CV4 [P1–064], which denote the coordination number of the P1 phosphorus with respect to the O2 and O64 oxygen atoms, respectively, in the DIMP molecule. The CVs are shown in Figure 11(a), and the corresponding free energy

surface is depicted in Figure 11(b). The reaction mechanism takes place in two substeps, as shown in Figure 11(c). The reactant is described by CV3 = 0.80 and CV4 = 0.05, in which the P1–O2 and P1–O64 bond distances are 1.69 and 3.02 Å, respectively. The P1–O2 bond first stretches to 1.95 Å and forms the first transition state (TS1). The P1–O2 bond then dissociates to 2.46 and creates a stable intermediate, I (CV3 = 0.15, CV4 = 0.04), giving a free energy activation of 18.51 kJ/mol. The reaction proceeds over a second transition state (TS2) in which the P1–O2 bond is further stretched and the resulting –$OCHCH_3CH_3$ fragment binds to the surface Al atom. In the product state, the distance from the P1 atom to the surface oxygen (O64) shortens (1.74 Å), indicating the formation of a P1–O64 covalent bond. In contrast, the P1–O2 bond length further increases, showing the complete decomposition of the DIMP molecule.

Collectively, our AIMD calculations show that the decomposition of DIMP most likely progresses via a propene elimination on the alumina surface. The final step of the propene elimination occurs via the abstraction of a hydrogen atom by the surface oxygen atom of gamma-alumina. We also performed metadynamics simulations to evaluate the free energy activation of this process. The C-H coordination (CV5) and H–O coordination (CV6) were selected as collective variables, as shown in Figure S22 in the Supporting Information. A Gaussian with a height of 0.0001 Hartree was used for these simulations. Figure S23 in the Supporting Information illustrates free energy profiles for the C–H activation within the 200 – 500° C temperature range. In Figure S24, we show free energy profiles in the 600 – 900° C temperature range. The free energy profile at 1000° C is shown in Figure S25a, and Figure S25b summarizes the free energy activation barrier as a function of temperature. The free energy activation barriers range from 3.91 – 1.29 kJ/mol for the 200 – 1000° C temperature range. We find that the free energy activation barrier value decreases with increasing the temperature. The small free energy barrier value in the 600 – 1000° C temperature range lies between 5 – 28 kJ/mol, which can be easily accessible by experiment. Our theoretical findings are also consistent with experimental studies, which also identified propene as the

main gas-phase product of the DIMP decomposition. In summary, our AIMD simulations show that the γ-Al_2O_3 surface can trap and subsequently decompose DIMP due to strong electrostatic attractions between the phosphoryl oxygen and surface Al atoms.

Conclusions

In this work, we have harnessed large-scale *ab initio* molecular dynamics calculations to investigate the adsorption and decomposition of DIMP on the γ-alumina surface over a wide range of temperatures. Our DFT-based molecular dynamics calculations predict a spontaneous decomposition of DIMP with propene as the main by-product within the 700 – 1000° C temperature range (the decomposition reaction leads to propene and an Al–$OCHCH_3CH_3$ adsorbate at 700° C). Due to the short-time scales inherent to BOMD simulations, it is likely that a similar decomposition would also occur at lower temperatures but would take longer to happen. Well-tempered metadynamics AIMD simulations were performed for temperatures ranging from 200 – 1000° C to provide atomistic-level details of the reaction path and associated energetics of DIMP decomposition. Our metadynamics calculations also reveal that the free energy barrier value decreases with temperature. The low free energy barrier values at higher temperatures suggest that that reaction is extremely fast at higher temperatures and is likely to occur at a lower rate at lower temperatures.

In our study, we obtained free energy values of 62.75 to 5.24 kJ/mol within the 200 – 1000° C temperature range. Recent experiments on CWAs have also been carried out under similar temperatures, including vapor phase decomposition of DMMP (a sarin surrogate) at 500 – 800 K,[58] sarin decomposition on TiO_2 nanoparticles at 1000 K,[53] and decomposition of CWAs at 2000 K.[31,59,60] Collectively, all of these experiments showed that the temperature ranges studied in this work can also be achieved under operational conditions, and DIMP would decompose on the γ-Al_2O_3 surface. Due to the structural similarity between DIMP and sarin, our calculations provide additional insight into decomposition mechanisms of both

these molecules and elucidate atomic details of sarin decomposition on candidate metal-oxide surfaces. As a final remark, this study serves as a convincing demonstration of the use of DFT-based molecular dynamics simulations for investigating the interactions of CWAs with existing metal-oxides, which can be used to guide experimental efforts on these hazardous compounds.

Acknowledgement

The project or effort depicted was or is sponsored by the Department of the Defense, Defense Threat Reduction Agency under the Materials Science in Extreme Environments University Research Alliance, HDTRA1-20-2-0001. The content of the information does not necessarily reflect the position or the policy of the federal government, and no official endorsement should be inferred.

Supporting Information Available

Additional materials on free energy profiles, fluctuations of collective variables, convergence tests of metadynamics calculations, and fluctuations of the C–O bond distance in DIMP from metadynamics calculations.

References

(1) Kim, K.; Tsay, O. G.; Atwood, D. A.; Churchill, D. G. Destruction and Detection of Chemical Warfare Agents. *Chem. Rev.* **2011**, *111*, 5345–5403.

(2) Picard, B.; Chataigner, I.; Maddaluno, J.; Legros, J. Introduction to chemical warfare agents, relevant simulants and modern neutralisation methods. *Org. Biomol. Chem.* **2019**, *17*, 6528–6537.

(3) Michalkova, A.; Paukku, Y.; Majumdar, D.; Leszczynski, J. Theoretical study of adsorption of tabun on calcium oxide clusters. *Chem. Phys. Lett.* **2007**, *438*, 72–77.

(4) Wagner, G. W.; Koper, O. B.; Lucas, E.; Decker, S.; Klabunde, K. J. Reactions of VX, GD, and HD with Nanosize CaO: Autocatalytic Dehydrohalogenation of HD. *J. Phys. Chem. B* **2000**, *104*, 5118–5123.

(5) Michalkova, A.; Ilchenko, M.; Gorb, L.; Leszczynski, J. Theoretical Study of the Adsorption and Decomposition of Sarin on Magnesium Oxide. *J. Phys. Chem. B* **2004**, *108*, 5294–5303.

(6) Wagner, G. W.; Bartram, P. W.; Koper, O.; Klabunde, K. J. Reactions of VX, GD, and HD with Nanosize MgO. *J. Phys. Chem. B* **1999**, *103*, 3225–3228.

(7) Mahato, T.; Prasad, G.; Singh, B.; Acharya, J.; Srivastava, A.; Vijayaraghavan, R. Nanocrystalline zinc oxide for the decontamination of sarin. *J. Hazard. Mater.* **2009**, *165*, 928–932.

(8) Prasad, G.; Mahato, T.; Singh, B.; Ganesan, K.; Pandey, P.; Sekhar, K. Detoxification reactions of sulphur mustard on the surface of zinc oxide nanosized rods. *J. Hazard. Mater.* **2007**, *149*, 460–464.

(9) Prasad, G.; Ramacharyulu, P.; Singh, B.; Batra, K.; Srivastava, A. R.; Ganesan, K.; Vijayaraghavan, R. Sun light assisted photocatalytic decontamination of sulfur mustard using ZnO nanoparticles. *J. Mol. Catal. A: Chem.* **2011**, *349*, 55–62.

(10) Hirakawa, T.; Sato, K.; Komano, A.; Kishi, S.; Nishimoto, C. K.; Mera, N.; Kugishima, M.; Sano, T.; Ichinose, H.; Negishi, N.; Seto, Y.; Takeuchi, K. Experimental Study on Adsorption and Photocatalytic Decomposition of Isopropyl Methylphosphonofluoridate at Surface of TiO_2 Photocatalyst. *J. Phys. Chem. C* **2010**, *114*, 2305–2314.

(11) Prasad, G. K.; Mahato, T. H.; Singh, B.; Ganesan, K.; Srivastava, A. R.; Kaushik, M. P.; Vijayraghavan, R. Decontamination of sulfur mustard and sarin on titania nanotubes. *AIChE Journal* **2008**, *54*, 2957–2963.

(12) Prasad, G.; Singh, B.; Ganesan, K.; Batra, A.; Kumeria, T.; Gutch, P.; Vijayaraghavan, R. Modified titania nanotubes for decontamination of sulphur mustard. *J. Hazard. Mater.* **2009**, *167*, 1192–1197.

(13) Ramacharyulu, P.; Prasad, G.; Ganesan, K.; Singh, B. Photocatalytic decontamination of sulfur mustard using titania nanomaterials. *J. Mol. Catal. A: Chem.* **2012**, *353-354*, 132–137.

(14) Sato, K.; Hirakawa, T.; Komano, A.; Kishi, S.; Nishimoto, C. K.; Mera, N.; Kugishima, M.; Sano, T.; Ichinose, H.; Negishi, N.; Seto, Y.; Takeuchi, K. Titanium dioxide photocatalysis to decompose isopropyl methylphosphonofluoridate (GB) in gas phase. *Appl. Catal. B: Environ.* **2011**, *106*, 316–322.

(15) Štengl, V.; Grygar, T. M.; Opluštil, F.; Němec, T. Ge4+ doped TiO_2 for stoichiometric degradation of warfare agents. *J. Hazard. Mater.* **2012**, *227-228*, 62–67.

(16) Wagner, G. W.; Chen, Q.; Wu, Y. Reactions of VX, GD, and HD with Nanotubular Titania. *J. Phys. Chem. C* **2008**, *112*, 11901–11906.

(17) Kuiper, A.; van Bokhoven, J.; Medema, J. The role of heterogeneity in the kinetics of a surface reaction: I. Infrared characterization of the adsorption structures of organophosphonates and their decomposition. *J. Catal.* **1976**, *43*, 154–167.

(18) Saxena, A.; Sharma, A.; Srivastava, A. K.; Singh, B.; Gutch, P. K.; Semwal, R. P. Kinetics of adsorption of sulfur mustard on Al_2O_3 nanoparticles with and without impregnants. *J. Chem. Technol. Biotechnol.* **2009**, *84*, 1860–1872.

(19) Saxena, A.; Srivastava, A. K.; Singh, B.; Gupta, A. K.; Suryanarayana, M. V.; Pandey, P. Kinetics of adsorptive removal of DEClP and GB on impregnated Al_2O_3 nanoparticles. *J. Hazard. Mater.* **2010**, *175*, 795–801.

(20) Wagner, G. W.; Procell, L. R.; O'Connor, R. J.; Munavalli, S.; Carnes, C. L.; Kapoor, P. N.; Klabunde, K. J. Reactions of VX, GB, GD, and HD with Nanosize Al_2O_3. Formation of Aluminophosphonates. *J. Am. Chem. Soc.* **2001**, *123*, 1636–1644.

(21) Walenta, C. A.; Xu, F.; Tesvara, C.; O'Connor, C. R.; Sautet, P.; Friend, C. M. Facile Decomposition of Organophosphonates by Dual Lewis Sites on a Fe_3O_4(111) Film. *J. Phys. Chem. C* **2020**, *124*, 12432–12441.

(22) Trotochaud, L.; Tsyshevsky, R.; Holdren, S.; Fears, K.; Head, A. R.; Yu, Y.; Karslıoğlu, O.; Pletincx, S.; Eichhorn, B.; Owrutsky, J.; Long, J.; Zachariah, M.; Kuklja, M. M.; Bluhm, H. Spectroscopic and Computational Investigation of Room-Temperature Decomposition of a Chemical Warfare Agent Simulant on Polycrystalline Cupric Oxide. *Chem. Mater.* **2017**, *29*, 7483–7496.

(23) Digne, M.; Sautet, P.; Raybaud, P.; Euzen, P.; Toulhoat, H. Use of DFT to achieve a rational understanding of acid–basic properties of γ-alumina surfaces. *J. Catal.* **2004**, *226*, 54–68.

(24) Gu, J.; Wang, J.; Leszczynski, J. Structure and Energetics of (111) Surface of γ-Al_2O_3: Insights from DFT Including Periodic Boundary Approach. *ACS Omega* **2018**, *3*, 1881–1888.

(25) Roy, S.; Mpourmpakis, G.; Hong, D.-Y.; Vlachos, D. G.; Bhan, A.; Gorte, R. J. Mechanistic Study of Alcohol Dehydration on γ-Al_2O_3. *ACS Catal.* **2012**, *2*, 1846–1853.

(26) Christiansen, M. A.; Mpourmpakis, G.; Vlachos, D. G. Density Functional Theory-Computed Mechanisms of Ethylene and Diethyl Ether Formation from Ethanol on γ-Al_2O_3(100). *ACS Catal.* **2013**, *3*, 1965–1975.

(27) Bermudez, V. M. Quantum-Chemical Study of the Adsorption of DMMP and Sarin on γ-Al_2O_3. *J. Phys. Chem. C* **2007**, *111*, 3719–3728.

(28) Bailin, L. J.; Sibert, M. E.; Jonas, L. A.; Bell, A. T. Microwave decomposition of toxic vapor simulants. *Environ. Sci. Technol.* **1975**, *9*, 254–258.

(29) Gibson, K. D.; Sibener, S. J. Fate of Some Chemical Warfare Simulants Adsorbed on an Inert Surface when Exposed to Rapid Laser Initiated Heating. *J. Phys. Chem. C* **2018**, *122*, 24684–24689.

(30) Thompson, R. S.; Brann, M. R.; Purdy, E. H.; Graham, J. D.; McMillan, A. A.; Sibener, S. J. Rapid Laser-Induced Temperature Jump Decomposition of the Nerve Agent Simulant Diisopropyl Methylphosphonate under Atmospheric Conditions. *J. Phys. Chem. C* **2019**, *123*, 21564–21570.

(31) Senyurt, E. I.; Schoenitz, M.; Dreizin, E. L. Rapid destruction of sarin surrogates by gas phase reactions with focus on diisopropyl methylphosphonate (DIMP). *Def. Technol.* **2021**, *17*, 703–714.

(32) Glaude, P.; Melius, C.; Pitz, W.; Westbrook, C. Detailed chemical kinetic reaction mechanisms for incineration of organophosphorus and fluoroorganophosphorus compounds. *Proc. Combust. Inst.* **2002**, *29*, 2469–2476.

(33) VandeVondele, J.; Krack, M.; Mohamed, F.; Parrinello, M.; Chassaing, T.; Hutter, J. QUICKSTEP: Fast and accurate density functional calculations using a mixed Gaussian and plane waves approach. *Comput. Phys. Commun.* **2005**, *167*, 103–128.

(34) Perdew, J. P.; Burke, K.; Ernzerhof, M. Generalized Gradient Approximation Made Simple. *Phys. Rev. Lett.* **1996**, *77*, 3865–3868.

(35) Grimme, S. Semiempirical GGA-type density functional constructed with a long-range dispersion correction. *J. Comput. Chem.* **2006**, *27*, 1787–1799.

(36) Goedecker, S.; Teter, M.; Hutter, J. Separable dual-space Gaussian pseudopotentials. *Phys. Rev. B* **1996**, *54*, 1703–1710.

(37) Hartwigsen, C.; Goedecker, S.; Hutter, J. Relativistic separable dual-space Gaussian pseudopotentials from H to Rn. *Phys. Rev. B* **1998**, *58*, 3641–3662.

(38) Cholewinski, M. C.; Dixit, M.; Mpourmpakis, G. Computational Study of Methane Activation on γ-Al_2O_3. *ACS Omega* **2018**, *3*, 18242–18250.

(39) Dixit, M.; Kostetskyy, P.; Mpourmpakis, G. Structure–Activity Relationships in Alkane Dehydrogenation on γ-Al_2O_3: Site-Dependent Reactions. *ACS Catal.* **2018**, *8*, 11570–11578.

(40) VandeVondele, J.; Hutter, J. An efficient orbital transformation method for electronic structure calculations. *J. Chem. Phys.* **2003**, *118*, 4365–4369.

(41) Kolafa, J. Time-reversible always stable predictor–corrector method for molecular dynamics of polarizable molecules. *J. Comput. Chem.* **2004**, *25*, 335–342.

(42) Kühne, T. D.; Krack, M.; Mohamed, F. R.; Parrinello, M. Efficient and Accurate Car-Parrinello-like Approach to Born-Oppenheimer Molecular Dynamics. *Phys. Rev. Lett.* **2007**, *98*, 066401.

(43) Nosé, S. A unified formulation of the constant temperature molecular dynamics methods. *J. Chem. Phys.* **1984**, *81*, 511–519.

(44) Hoover, W. G. Canonical dynamics: Equilibrium phase-space distributions. *Phys. Rev. A* **1985**, *31*, 1695–1697.

(45) Digne, M.; Sautet, P.; Raybaud, P.; Euzen, P.; Toulhoat, H. Hydroxyl Groups on γ-Alumina Surfaces: A DFT Study. *J. Catal.* **2002**, *211*, 1–5.

(46) Wilson, S. The dehydration of boehmite, γ-AlOOH, to γ-Al_2O_3. *J. Solid State Chem.* **1979**, *30*, 247–255.

(47) Biswas, S.; Kwon, H.; Barsanti, K. C.; Myllys, N.; Smith, J. N.; Wong, B. M. Ab initio metadynamics calculations of dimethylamine for probing pKb variations in bulk vs. surface environments. *Phys. Chem. Chem. Phys.* **2020**, *22*, 26265–26277.

(48) Barducci, A.; Bussi, G.; Parrinello, M. Well-Tempered Metadynamics: A Smoothly Converging and Tunable Free-Energy Method. *Phys. Rev. Lett.* **2008**, *100*, 020603.

(49) Biswas, S.; Wong, B. M. Ab initio metadynamics calculations reveal complex interfacial effects in acetic acid deprotonation dynamics. *J. Mol. Liq.* **2021**, *330*, 115624.

(50) Mitchell, M. B.; Sheinker, V. N.; Mintz, E. A. Adsorption and Decomposition of Dimethyl Methylphosphonate on Metal Oxides. *J. Phys. Chem. B* **1997**, *101*, 11192–11203.

(51) Tsyshevsky, R.; Holdren, S.; Eichhorn, B. W.; Zachariah, M. R.; Kuklja, M. M. Sarin Decomposition on Pristine and Hydroxylated ZnO: Quantum-Chemical Modeling. *J. Phys. Chem. C* **2019**, *123*, 26432–26441.

(52) Tsyshevsky, R.; Head, A. R.; Trotochaud, L.; Bluhm, H.; Kuklja, M. M. Mechanisms of Degradation of Toxic Nerve Agents: Quantum-chemical Insight into Interactions of Sarin and Soman with Molybdenum Dioxide. *Surf. Sci.* **2020**, *700*, 121639.

(53) Tsyshevsky, R.; McEntee, M.; Durke, E. M.; Karwacki, C.; Kuklja, M. M. Degradation of Fatal Toxic Nerve Agents on Dry TiO_2. *ACS Appl. Mater. Interfaces* **2021**, *13*, 696–705.

(54) Wischert, R.; Copéret, C.; Delbecq, F.; Sautet, P. Dinitrogen: a selective probe for tri-coordinate Al "defect" sites on alumina. *Chem. Commun.* **2011**, *47*, 4890–4892.

(55) Zegers, E.; Fisher, E. Gas-Phase Pyrolysis of Diisopropyl Methylphosphonate. *Combust. Flame* **1998**, *115*, 230–240.

(56) Senyurt, E. I.; Schoenitz, M.; Dreizin, E. L. Rapid destruction of sarin surrogates by gas phase reactions with focus on diisopropyl methylphosphonate (DIMP). *Def. Technol.* **2020**,

(57) Yuan, B.; Eilers, H. T-jump pyrolysis and combustion of diisopropyl methylphosphonate. *Combust. Flame* **2019**, *199*, 69–84.

(58) Mukhopadhyay, S.; Schoenitz, M.; Dreizin, E. L. Vapor-phase decomposition of dimethyl methylphosphonate (DMMP), a sarin surrogate, in presence of metal oxides. *Def. Technol.* **2021**, *17*, 1095–1114.

(59) Neupane, S.; Barnes, F.; Barak, S.; Ninnemann, E.; Loparo, Z.; Masunov, A. E.; Vasu, S. S. Shock Tube/Laser Absorption and Kinetic Modeling Study of Triethyl Phosphate Combustion. *J. Phys. Chem. A* **2018**, *122*, 3829–3836.

(60) Mathieu, O.; Kulatilaka, W. D.; Petersen, E. L. Shock-tube studies of Sarin surrogates. *Shock Waves* **2019**, *29*, 441–449.

TOC graphic